ResearchGate

See discussions, stats, and author profiles for this publication at: https://www.researchgate.net/publication/244271755

Theoretical and experimental investigations on the structure and vibrational spectra of 4-{[(1 Z)-1-methyl-3-oxobut-1-enyl]amino}benzoic acid

ARTICLE *in* JOURNAL OF MOLECULAR STRUCTURE THEOCHEM · MAY 2005

Impact Factor: 1.37 · DOI: 10.1016/j.theochem.2004.12.041

READS

17

5 AUTHORS, INCLUDING:

Kaustubh A. Joshi

Institute of Chemical Technology, Mumbai

14 PUBLICATIONS **113** CITATIONS

SEE PROFILE

Megha Subhash Deshpande

Nara Institute of Science and Technology

14 PUBLICATIONS **215** CITATIONS

SEE PROFILE

Ray J. Butcher

Howard University

1,042 PUBLICATIONS **9,370** CITATIONS

SEE PROFILE

Shridhar Gejji

Savitribai Phule Pune University

118 PUBLICATIONS **1,243** CITATIONS

SEE PROFILE

Available from: Megha Subhash Deshpande

Retrieved on: 22 January 2016

ELSEVIER

Journal of Molecular Structure: THEOCHEM 722 (2005) 57–63

THEO CHEM

www.elsevier.com/locate/theochem

Theoretical and experimental investigations on the structure and vibrational spectra of 4-{[(1*Z*)-1-methyl-3-oxobut -1-enyl]amino}benzoic acid

Kaustubh A. Joshi[a], Megha S. Deshpande[a], Avinash S. Kumbhar[a], Ray J. Butcher[b], Shridhar P. Gejji[a,*]

[a]*Department of Chemistry, University of Pune, Pune 411007, India*
[b]*Department of Chemistry, Howard University, Washington, DC 20059, USA*

Received 8 October 2004; accepted 1 December 2004
Available online 14 March 2005

Abstract

Hartree–Fock and hybrid density functional methods have been used to determine the structure and energetics of 4-{[(1*Z*)-1-methyl-3-oxobut-1-enyl]amino}benzoic acid (**1**) tautomers. The N–H···O (1.750 Å) intramolecular hydrogen bonded interactions are present in the keto tautomer and relatively strong O–H···N (1.616 Å) interactions prevail in the enol form. The two functional groups, viz. benzoic acid and 4-amino-pent-3-ene-2-one orient mutually with 154° in the keto tautomer in agreement with the X-ray data. Extended conjugation, which renders stability to the keto tautomer, has been manifested in the topography of molecular electrostatic potential. The deepest minimum in the electrostatic potential of the lowest energy tautomer emerges near carbonyl oxygen and is located near the carboxylic oxygen of benzoic acid for the enol form. X-ray crystal structure reveals the extended three-dimensional network comprising of C═O···H intermolecular hydrogen bonds (1.82 Å). Quantum mechanically derived molecular electrostatic potential provide insights for the formation of supramolecular assemblies. The 1699 and 1240 cm^{-1} C═O and C–N stretching vibrations in the observed infrared spectrum agree well with those predicted from the density functional calculations. The downshift of OH stretching to ~2986 cm^{-1} in the observed infrared spectrum results from the C═O···H intermolecular hydrogen bonded interactions.
© 2005 Elsevier B.V. All rights reserved.

Keywords: Hartree–Fock; Hybrid density functional; Hydrogen bonding; Molecular electrostatic potential

1. Introduction

Schiff base ligands and their metal complexes, have been of considerable interest in the literature owing to their numerous applications as anticancer drugs or in analytical chemistry [1–6]. Salen-type symmetrical ligands act as catalysts in the asymmetric Diels–Alder reaction, epoxidation of olefins, oxidation of sulfides and cyclopropanation. Bhattacharya and co-workers [7] have reported a new water-soluble Co-salen complex, which facilitates spontaneous cleavage of DNA under ambient aerobic conditions. A functionalised Cu-salen complex and its binding to DNA has been investigated by Routier et al. [8]. On the other hand the papers reporting unsymmetrical bidentate Schiff base type ligands, which are potentially important synthons for the asymmetric or chiral bidentate systems with numerous applications in enantioselective catalysis, are relatively scanty [9,10]. In this regard unsymmetrical Schiff base ligands derived from diketones have not yet been explored. As a pursuit of this in the present work we study a new type of bidentate ligand **1**, comprising of 4-amino benzoic acid and 2,4 pentanedione units. The C═O···H and N···H–O interactions in the keto and enol tautomers of **1** are investigated. We derive the electronic structure, charge distributions and vibrational spectra of the titled ligand employing the quantum chemical and hybrid density functional methods. The synthesis and the structural parameters determined from the single crystal X-ray diffraction experiment have been presented. The experimental and computational methods are outlined below.

* Corresponding author. Tel./fax: +91 20 25691728.
E-mail address: spgejji@chem.unipune.ernet.in (S.P. Gejji).

0166-1280/$ - see front matter © 2005 Elsevier B.V. All rights reserved.
doi:10.1016/j.theochem.2004.12.041

2. Experimental

2.1. Synthesis of (1)

2,4-Pentanedione (0.5 g, 0.005 M) was added dropwise with stirring to 4-amino benzoic acid (0.68 g, 0.005 M) in dry methanol with catalytic amount of formic acid. The solution was stirred for 2 h and heated further for 3 h, which is followed by stirring at ambient temperature for 24 h. After cooling and filtering the solution, the yellow crystals of **1** (Yield = 60%, m.p. = 182 °C) suitable for X-ray diffraction were obtained. The infrared spectrum was recorded as KBr pellet on a Shimadzu FTIR-8400 spectrophotometer. NMR spectrum (given below) was recorded in DMSO-d_6 on a Varian 300 MHz spectrometer: ^{1}H-NMR (DMSO-d_6 solvent, room temperature, ppm): 12.68 (1H, s), 7.98 (2H, d), 7.35 (2H, d), 5.41 (1H, s), 2.57 (1H, s), 2.21 (3H, s), 2.10 (3H, s).

2.2. X-ray Crystallography

A crystal of **1** obtained by slow evaporation of the reaction mixture with a size of $0.60\times0.30\times0.20$ mm^3 was attached in a random orientation to the end of a glass fibre using epoxy cement and transferred to a goniometer head. The X-ray diffraction measurements were performed on a Bruker 1K SMART CCD diffractometer with graphite-monochromated Mo Kα radiation ($\lambda = 0.71073$ Å). The structure was solved by direct methods and subjected to full-matrix least squares refinement on F^2 using the SMART and SHELXTL programs [11]. The hydrogens were partially located from difference electron-density maps, and the rest were fixed at calculated positions. Some details of data collection and refinement are given in Table 3.

3. Computational method

LCAO-MO-SCF restricted Hartree–Fock (HF) calculations were carried out on different tautomers of **1** employing the GAUSSIAN 94 programme [12]. The internally stored 6-31G(d,p) basis set was used. Stationary point geometries with respect to the nuclear coordinates were obtained by the simultaneous relaxation of all the geometric parameters using the analytical gradient method [13]. These geometries were subjected to optimizations using the hybrid density functional method incorporating the Becke's three-parameter exchange with correlation functional given by Lee et al. (B3LYP) [14,15].

The molecular electrostatic potential (MESP) $V(\mathbf{r})$ at a point $\mathbf{r}$ due to a molecular system with nuclear charges $\{Z_A\}$ located at $\{R_A\}$ and the electron density $\rho(\mathbf{r})$ is given by

$$V(\mathbf{r}) = \sum_{A=1}^{N} \frac{Z_A}{|\mathbf{r}-\mathbf{R}_A|} - \int \frac{\rho(\mathbf{r}')\mathrm{d}^3\mathbf{r}'}{|\mathbf{r}-\mathbf{r}'|} \quad (1)$$

In Eq. (1) N denotes the total number of nuclei in the molecule and the two terms refer to the bare nuclear potential and the electronic contributions, respectively. The balance of these two terms brings about the effective localization of electron-rich regions in the molecular system. The MESP topography is mapped by examining the eigenvalues of the Hessian matrix at the point where the gradient $V(\mathbf{r})$ vanishes. The MESP critical points (CPs) were located. Fortran program UNIVIS-2000 [16–18] was used for visualization of the MESP topography. The CPs can be characterized [19] in terms of an ordered pair of (rank, signature), which can further be grouped into three sets, viz. (3, +3), (3, +1) and (3, −1). The (3, +3) CPs corresponds to the minima whereas the remaining ones turn out to be the saddle points. These CPs represent potential cation binding sites. Harmonic vibrational frequencies were calculated from the diagonalization of force constant matrix. The stationary point geometries thus obtained were confirmed to be the local minima on the potential energy surface since all the vibrational frequencies turn out to be real. Normal vibrations were assigned by visualizing the displacement of atoms around their equilibrium positions.

4. Results and discussion

Optimized geometries of tautomers of **1** along with the atomic labels are displayed in Fig. 1. The HF and B3LYP relative stabilization energies and their corresponding zero point energy (zpe) corrected values of the *keto* and *enol* tautomers are given in Table 1. The zero energy for the lowest energy *keto* tautomer corresponds to −741.083106 au in the HF calculations with the corresponding zero point energy corrected value being −740.834438 au. As may

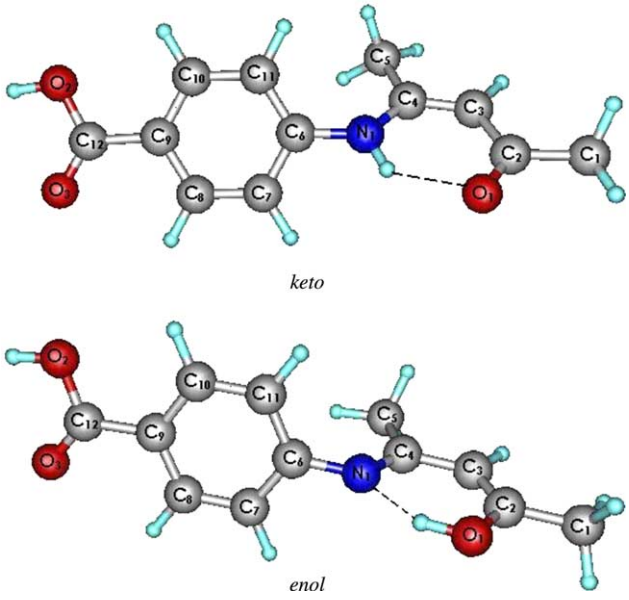

Fig. 1. The optimized geometries of the keto and enol forms of **1**.

Table 1
Relative stabilization energies (in kJ mol^{-1}) for the tautomers of *1*

	Keto	Enol
HF	0.0(0.0)	20.8(20.9)
B3LYP	0.0(0.0)	19.5(17.2)

Zero point corrected values are given in parentheses.

readily be noticed the *keto* form is 20.9 kJ mol^{-1} lower in energy than the *enol* tautomer within the HF framework. Within the framework of the B3LYP theory this energy difference turns out to be 17.2 kJ mol^{-1}.

The geometrical parameters of these tautomers are given in Table 2 along with their experimental counterparts. The observed CN and CO bond lengths in a crystal are in good agreement with those predicted from the theoretical calculations for a gas phase structure, with largest deviation of 0.045 Å predicted for the $C_{12}O_2$ bond distance. Bond angles predicted from the B3LYP/6-31G (d,p) calculations generally agree within 3° except for the $C_7C_8N_1$, which shows a largest deviation (8°). Thus C═O···H intermolecular interactions present in a crystal results in the opening of the $C_7C_8N_1$ bond angle compared to the gas phase structure derived from the B3LYP calculations. B3LYP theory predicts that the benzoic acid and the 4-amino-pent-3-ene-2-one in **1** orient mutually with an angle of 26° for the lowest energy tautomer in agreement with the X-ray diffraction experiment wherein the $C_7C_6N_1C_4$ dihedral angle has been observed to be 158°. On the other hand in the enol tautomer, where the conjugation has been extended to a lesser extent relative to the lowest energy configuration, the deviation from planarity has further been increased; the two functional groups orient mutually by 48°.

Table 2
B3LYP and HF optimized geometrical parameters (bond lengths in Å and bond angles in °) for tautomers of **1**

	B3LYP		HF		Expt
	Keto	Enol	Keto	Enol	
$r(O_1C_2)$	1.247	1.326	1.212	1.319	1.251(3)
$r(O_2C_{12})$	1.360	1.360	1.330	1.331	1.315(3)
$r(O_2H)$	0.971	0.971	0.948	0.948	0.820
$r(O_3C_{12})$	1.216	1.216	1.191	1.192	1.206(3)
$r(N_1C_4)$	1.365	1.310	1.357	1.272	1.349(4)
$r(N_1C_6)$	1.397	1.400	1.404	1.404	1.397(3)
$r(N_1H)$	1.033	–	1.001		0.943
$r(C_1C_2)$	1.519	1.498	1.513	1.496	1.496(4)
$r(C_2C_3)$	1.446	1.373	1.455	1.345	1.414(4)
$r(C_3C_4)$	1.380	1.441	1.358	1.461	1.383(4)
$r(C_4C_5)$	1.506	1.514	1.508	1.512	1.489(4)
$r(C_6C_7)$	1.411	1.409	1.394	1.393	1.392(3)
$r(C_6C_{11})$	1.407	1.408	1.391	1.392	1.396(4)
$r(C_7C_8)$	1.384	1.386	1.378	1.379	1.391(4)
$r(C_8C_9)$	1.403	1.403	1.390	1.391	1.377(4)
$r(C_9C_{10})$	1.400	1.402	1.388	1.390	1.388(4)
$r(C_9C_{12})$	1.480	1.481	1.483	1.482	1.488(4)
$r(C_{10}C_{11})$	1.391	1.390	1.382	1.382	1.378(4)
$a(C_{12}O_2H)$	105.5	105.4	107.9	107.8	109.5
$a(C_4N_1C_6)$	132.6	125.2	129.6	123.6	132.1(2)
$a(C_4N_1H)$	110.5	–	113.4	–	111(2)
$a(O_1C_2C_3)$	123.2	122.4	123.7	124.3	122.6(2)
$a(O_1C_2C_1)$	119.4	113.9	119.8	112.3	118.6(3)
$a(C_4C_3C_2)$	124.1	122.7	124.5	124.3	125.0(3)
$a(N_1C_4C_3)$	119.3	118.3	121.6	119.9	118.9(2)
$a(N_1C_4C_5)$	120.9	124.6	119.2	125.1	121.0(3)
$a(C_7C_6N_1)$	116.5	118.3	118.0	119.7	124.7(2)
$a(C_8C_9C_{12})$	118.4	118.3	118.4	118.4	121.2(2)
$a(C_{10}C_9C_{12})$	122.7	122.5	122.3	122.3	119.6(3)
$a(O_3C_{12}O_2)$	121.8	121.7	121.9	121.7	123.3(3)
$a(O_3C_{12}C_9)$	125.1	125.1	124.6	124.7	123.5(2)
$a(O_2C_{12}C_9)$	113.2	113.2	113.6	113.6	113.2(2)
$d(C_7C_6N_1C_4)$	154.5	132.1	133.0	104.2	158.5(3)
$d(C_{11}C_6N_1C_4)$	28.4	52.9	50.5	80.1	25.3(4)

The titled ligand crystallizes in the monoclinic space group $P2(1)$ and the unit cell dimensions and other details pertaining to the data collection and refinement are listed in Table 3. Fig. 2 displays the crystal structure. The fractional atomic coordinates for non-hydrogen atoms are collected in Table 4, while the anisotropic thermal parameters are tabulated in Table 5. Two dimensional hydrogen bonded sheet of **1** viewed down the *b*-axis is shown in Fig. 3. The Figure shows presence of C═O···H′ interactions with the intermolecular distance of 1.82 Å. N–H···O intermolecular

Table 3
Crystal data and structure refinement for **1**

Identification code	md2	
Empirical formula	$C_{12}H_{13}NO_3$	
Formula weight	219.23	
Temperature	293(2) K	
Wavelength	1.54178 Å	
Crystal system	Monoclinic	
Space group	$P2(1)$	
Unit cell dimensions	$a=7.8992(5)$ Å	$\alpha=90°$
	$b=8.7619(6)$ Å	$\beta=90.504(4)°$
	$c=16.2214(12)$ Å	$\gamma=90°$
Volume	1122.67(13) Å^3	
Z	4	
Density (calculated)	1.297 mg/m^3	
Absorption coefficient	0.774 mm^{-1}	
$F(000)$	464	
Crystal size	0.60×0.30×0.20 mm^3	
θ range for data collection	5.60–69.03°	
Index ranges	$-9\le h\le 0$, $0\le k\le 10$, $-19\le l\le 19$	
Reflections collected	2242	
Independent reflections	2141 [R(int)=0.0407]	
Completeness to $\theta=69.03°$	95.2%	
Absorption correction	None	
Refinement method	Full-matrix least-squares on F^2	
Data/restraints/parameters	2141/1/297	
Goodness-of-fit on F^2	1.041	
Final R indices [$I>2\sigma(I)$]	$R1=0.0351$, $wR2=0.0932$	
R indices (all data)	$R1=0.0381$, $wR2=0.0962$	
Absolute structure parameter	0.0(3)	
Extinction coefficient	0.0036(15)	
Largest difference peak and hole	0.093 and −0.096 e Å^{-3}	

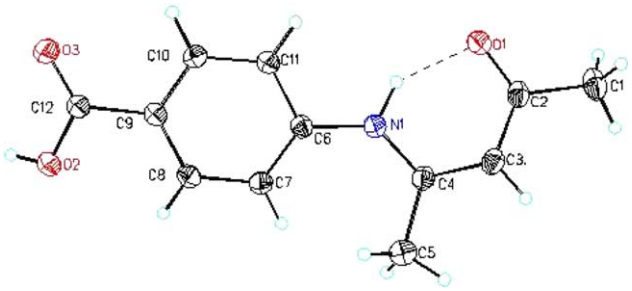

Fig. 2. ORTEP diagram of *1*.

hydrogen bonded interactions (H···O distance = 0.82 Å) are observed in the crystal of the title ligand.

The residual atomic charges derived from the electrostatic potential on different centers in *keto* and *enol* tautomers are displayed in Table 6. As may be seen the C_3 center turns out to be most electron-rich in both these tautomers and the N_1 turns out to be relatively electron rich than O_1 and O_2 centres (with the respective residual charges being −0.696 and −0.677) in the keto tautomer. As pointed out earlier, the MESP brings about the effective localization of electron-rich regions in a molecular system.

Table 4
Atomic coordinates ($\times 10^4$) and equivalent isotropic displacement parameters (Å$^2 \times 10^3$) for **1**

	x	*y*	*z*	U(eq)
O(1A)	997(2)	9100(2)	600(1)	58(1)
O(2A)	−2137(3)	14,587(3)	4737(1)	70(1)
O(3A)	−1800(3)	16,166(3)	3682(1)	79(1)
O(1B)	6187(3)	16,482(2)	−4340(1)	63(1)
O(2B)	2005(3)	10,699(3)	−713(1)	64(1)
O(3B)	2640(3)	12,341(3)	289(1)	66(1)
N(1A)	857(3)	9892(3)	2160(1)	49(1)
N(1B)	4999(3)	16,184(3)	−2831(1)	47(1)
C(1A)	2103(4)	6697(4)	216(2)	74(1)
C(2A)	1580(3)	7850(3)	844(2)	52(1)
C(3A)	1815(3)	7506(3)	1689(2)	54(1)
C(4A)	1486(3)	8496(3)	2333(2)	49(1)
C(5A)	1900(4)	8043(4)	3196(2)	72(1)
C(6A)	302(3)	11,081(3)	2664(1)	45(1)
C(7A)	−305(3)	10,896(3)	3461(2)	57(1)
C(8A)	−915(3)	12,151(4)	3891(2)	55(1)
C(9A)	−945(3)	13,580(3)	3538(2)	48(1)
C(10A)	−335(3)	13,767(3)	2744(2)	54(1)
C(11A)	279(3)	12,534(3)	2312(2)	51(1)
C(12A)	−1653(3)	14,915(3)	3984(2)	52(1)
C(1B)	6898(3)	18,941(2)	−4855(1)	79(1)
C(2B)	6237(3)	17,892(2)	−4204(1)	53(1)
C(3B)	5707(3)	18,537(2)	−3448(1)	53(1)
C(4B)	5138(3)	17,711(3)	−2783(2)	47(1)
C(5B)	4651(4)	18,536(4)	−2016(2)	67(1)
C(6B)	4479(3)	15,122(3)	−2230(1)	43(1)
C(7B)	3534(3)	13,867(3)	−2486(1)	47(1)
C(8B)	2964(3)	12,813(3)	−1919(1)	47(1)
C(9B)	3325(3)	13,012(3)	−1082(1)	44(1)
C(10B)	4348(3)	14,222(3)	−845(1)	47(1)
C(11B)	4937(3)	15,262(3)	−1408(1)	48(1)
C(12B)	2638(3)	11,993(3)	−435(2)	48(1)

U(eq) is defined as one third of the trace of the orthogonalized U^{ij} tensor.

Table 5
Anisotropic displacement parameters (Å$^2 \times 10^3$) for **1**

	U^{11}	U^{22}	U^{33}	U^{23}	U^{13}	U^{12}
O(1A)	67(1)	58(1)	51(1)	0(1)	9(1)	0(1)
O(2A)	103(2)	63(1)	45(1)	2(1)	18(1)	18(1)
O(3A)	120(2)	55(1)	62(1)	8(1)	28(1)	22(1)
O(1B)	84(1)	53(1)	52(1)	−3(1)	18(1)	2(1)
O(2B)	84(1)	58(1)	52(1)	4(1)	11(1)	−9(1)
O(3B)	90(1)	68(1)	40(1)	8(1)	−2(1)	4(1)
N(1A)	56(1)	46(1)	45(1)	−1(1)	6(1)	1(1)
N(1B)	57(1)	44(1)	40(1)	−4(1)	8(1)	−2(1)
C(1A)	81(2)	67(2)	74(2)	−21(2)	22(2)	−7(2)
C(2A)	50(1)	46(1)	61(2)	−8(1)	14(1)	−6(1)
C(3A)	56(1)	41(1)	65(2)	0(1)	9(1)	1(1)
C(4A)	51(1)	43(1)	54(1)	3(1)	10(1)	−3(1)
C(5A)	91(2)	64(2)	62(2)	7(2)	4(1)	13(2)
C(6A)	46(1)	45(1)	43(1)	−3(1)	2(1)	−2(1)
C(7A)	73(2)	46(1)	51(1)	6(1)	13(1)	0(1)
C(8A)	65(1)	57(2)	44(1)	3(1)	14(1)	2(1)
C(9A)	51(1)	50(1)	43(1)	−1(1)	2(1)	1(1)
C(10A)	64(2)	46(1)	50(1)	6(1)	6(1)	6(1)
C(11A)	59(1)	51(2)	43(1)	4(1)	8(1)	6(1)
C(12A)	58(1)	53(2)	44(1)	0(1)	2(1)	5(1)
C(1B)	94(2)	71(2)	72(2)	19(2)	17(2)	1(2)
C(2B)	56(1)	52(1)	51(1)	4(1)	4(1)	2(1)
C(3B)	58(1)	44(1)	57(1)	0(1)	−1(1)	1(1)
C(4B)	48(1)	43(1)	49(1)	−4(1)	0(1)	4(1)
C(5B)	88(2)	54(2)	59(2)	−11(1)	5(1)	15(2)
C(6B)	43(1)	45(1)	41(1)	−4(1)	6(1)	3(1)
C(7B)	56(1)	48(1)	37(1)	−3(1)	−2(1)	0(1)
C(8B)	52(1)	46(1)	44(1)	−2(1)	−1(1)	−1(1)
C(9B)	44(1)	46(1)	41(1)	1(1)	2(1)	12(1)
C(10B)	50(1)	52(1)	40(1)	−5(1)	−3(1)	8(1)
C(11B)	48(1)	50(1)	46(1)	−5(1)	−3(1)	−1(1)
C(12B)	51(1)	50(1)	43(1)	4(1)	−2(1)	11(1)

The anisotropic displacement factor exponent takes the form: $-2\pi^2[h^2\, a^{*2}U^{11} + \ldots + 2\, hka^*b^*U^{12}]$.

Thus the MESP isosurface of $V = -177.2$ kJ mol^{-1} in **1** is depicted in Fig. 4 along with the (3, +3) MESP minima, labelled as x_1, x_2, etc. The (3, +3) CPs near oxygen and nitrogen centers in different tautomers along with their respective MESP values are given in Table 7. Accordingly the minimum near carbonyl oxygen of 4-amino-pent-3-ene-2-one in the keto tautomer turns out to be −265 kJ mol^{-1}

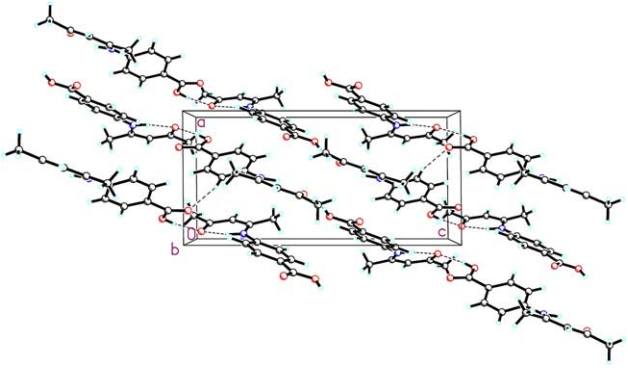

Fig. 3. Two-dimensional hydrogen bonded sheet of **1** viewed down the *b*-axis.

Table 6
Net atomic charges from the electrostatic potential in keto and enol tautomers of **1**

	Keto	Enol
C_1	−0.375	−0.338
C_2	0.934	0.687
C_3	−0.918	−0.852
C_4	0.689	0.771
C_5	−0.226	−0.238
C_6	0.505	−0.045
C_7	−0.297	−0.300
C_8	−0.051	0.542
C_9	−0.142	−0.169
C_{10}	−0.031	−0.031
C_{11}	−0.316	−0.306
C_{12}	0.823	0.834
N_1	−0.800	−0.754
O_1	−0.696	−0.628
O_2	−0.677	−0.682
O_3	−0.624	−0.631

compared to the deepest minimum found near the carboxylic oxygen (-224.8 kJ mol^{-1}) for the enol tautomer. Thus it may be inferred that the presence of extended conjugation, which renders more stability to the tautomer, has been pronounced in the keto tautomer. It may be concluded that the intermolecular C═O···H interactions in the keto form are facilitated via carbonyl oxygen of 4-amino-pent-3-ene-2-one in **1**, which is consistent with the extended hydrogen bonded network in a crystal (cf. Fig. 3). Thus the MESP topography may be used to gain insight for the molecular interactions in supramolecular assemblies.

Highest occupied molecular orbital (HOMO) (0.04 au isosurface) in both keto and enol tautomers derived from

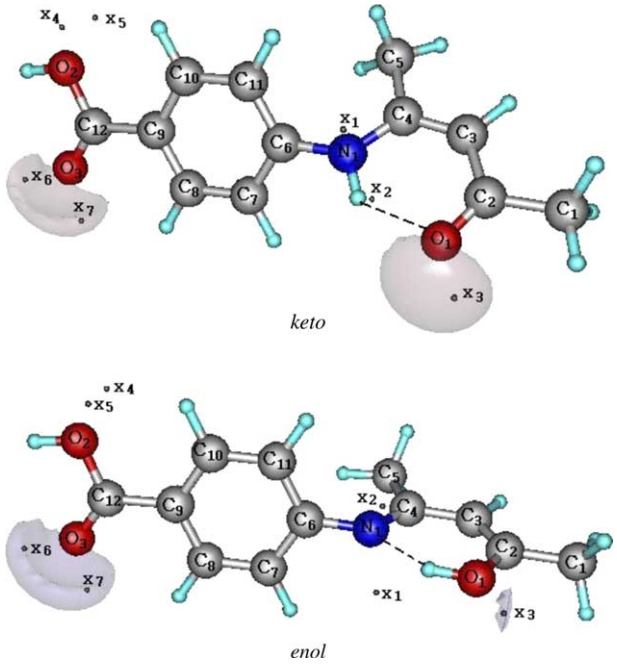

Fig. 4. MESP isosurface ($V=-177.2$ kJ mol^{-1}) and (3, +3) minima in different tautomers.

Table 7
The MESP minima (in kJ mol^{-1}) for tautomers of **1**

Atom		Keto	Enol
N_1	x_1	−18.5	−85.4
	x_2	−57.8	−83.1
O_1	x_3	−264.8	−185.0
O_2	x_4	−105.6	−121.0
	x_5	−105.4	−119.5
O_3	x_6	−211.1	−217.6
	x_7	−205.8	−224.4

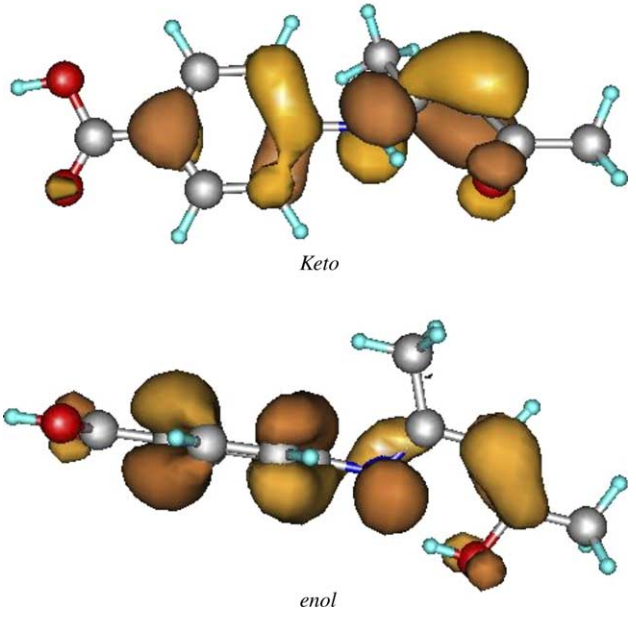

Fig. 5. Highest occupied molecular orbital (HOMO) (0.04 au isosurface) of keto and enol tautomers.

the HF/6-31G(d,p) wave function, are compared in Fig. 5. As is transparent a large overlap of p orbital of aromatic ring carbon with lone pair of nitrogen renders more stability to the keto tautomer over the enol tautomer. In order to attain

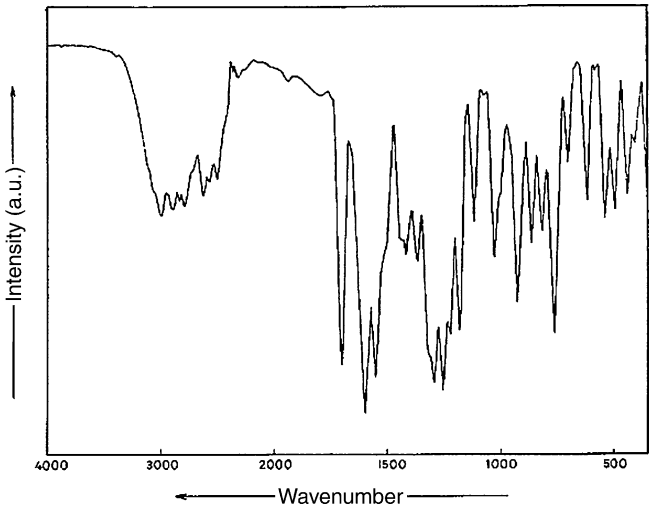

Fig. 6. Infrared spectrum of **1**.

Table 8
B3LYP/6-31G(d,p) calculated and the experimental vibrational frequencies (cm^{-1}) for **1**

Experimental	B3LYP	Assignment
2986 (38)	3532 (96)	O_2H stretch
	3050 (6)	$C_{11}H$, $C_{10}H$ stretch
	3021 (182)	N_1H stretch
	3020 (60)	C_8H stretch
	3019 (30)	$C_{10}H$ stretch
	3009 (13)	C_3H stretch
	2993 (3)	C_7H stretch
	2966 (8)	C_1H stretch
	2955 (12)	C_5H stretch
	2923 (9)	C_5H stretch
2887 (36)	2912 (12)	C_1H stretch
	2862 (8)	C_5H stretch
	2854 (5)	C_1H stretch
2779 (36)		
2617 (34)		
2563 (30)		
2496 (30)		
1699 (70)	1699 (366)	$C_{12}O_3$ stretch
1597 (80)	1589 (83)	C_2O_1 stretch
	1586 (511)	N_1H rock
1553 (72)	1556 (611)	C_7C_8, $C_{10}C_{11}$ stretch
	1511 (142)	C_8C_9, $C_{10}C_{11}$ stretch
	1469 (85)	$C_{10}C_{11}H$, C_9C_8H rock
1416 (45)	1442 (43)	C_8C_7H, C_6N_1H, C_4C_5H rock
	1410 (24)	HC_5H scissor
	1404 (14)	HC_5H scissor
	1397 (8)	HC_1H scissor
	1386 (34)	HC_1H scissor
1364 (46)	1369 (19)	$C_{10}C_{11}H$, C_6C_7H, C_9C_8H rock
	1338 (92)	C_4C_5H rock
	1321 (144)	N_1C_4 stretch + C_6N_1H, C_4C_5H rock
	1308 (33)	C_2C_1H rock
1290 (73)	1302 (424)	$C_{12}O_2$ stretch
	1279 (0)	C_6C_{11}, C_8C_9 stretch
1254 (74)	1258 (0)	C_6C_7H, C_9C_8H, $C_6C_{11}H$, $C_9C_{10}H$ rock
1221 (64)	1240 (426)	N_1C_6 stretch
1180 (60)	1189 (17)	C_9C_8H, C_6C_7H, C_6N_1H rock
	1151 (56)	$C_{12}O_2H$, C_8C_7H, C_6N_1H rock
	1139 (43)	C_2C_3H rock
1115 (37)	1118 (441)	$C_{12}O_2H$, $C_9C_{10}H$, C_7C_8H rock
	1077 (4)	C_9C_8H, C_6C_7H, $C_9C_{10}H$, $C_6C_{11}H$ rock
1026 (45)	1048 (189)	$C_{12}O_2$, C_8C_7H, $C_{11}C_{10}H$ rock
	995 (2)	C_5 methyl deformation
	984 (43)	C_5 methyl deformation
	975 (8)	C_1 methyl deformation
	965 (2)	$C_9C_{10}C_{11}$, $C_6C_7C_8$ bend
924 (55)	945 (45)	C_1 methyl deformation
	930 (0)	HC_7C_8H twist
	912 (2)	$HC_{10}C_{11}H$ twist
	892 (3)	$C_2C_3C_4$ bend
	879 (25)	$C_3C_2O_1$ bend
862 (41)	844 (122)	C_4N_1H wag
816 (40)	811 (12)	C_6C_7H, C_9C_8H, $C_6C_{11}H$, $C_9C_{10}H$ wag
	784 (2)	C_6C_7H, C_9C_8H, $C_6C_{11}H$, $C_9C_{10}H$ wag
	774 (1)	$C_7C_8C_9$, $C_6C_{11}C_{10}$ bend
762 (62)	732 (63)	C_4C_3H, $C_{12}O_2H$ wag
	725 (4)	C_4C_3H wag
700 (24)	708 (55)	$C_6N_1C_4$ bend
	666 (41)	
	635 (6)	$O_3C_{12}O_2$, $C_8C_9C_{10}$, $C_7C_6C_{11}$, $C_6N_1C_4$ bend
615 (32)	606 (0)	$C_6C_7C_8$, $C_9C_{10}C_{11}$ bend

effective overlap 4-amino-pent-3-ene-2-one relative to benzoic acid has been twisted further by 22° around the CN bond in the enol form. The extended conjugation in these tautomers is seen from Fig. 5. B3LYP predicted dipole moments of the gas phase structures of keto and enol tautomers turn out to be 4.402 and 4.169 D, respectively.

The measured infrared spectrum of **1** is shown in Fig. 6. The B3LYP calculated vibrational frequencies in 600–3550 cm^{-1} region, which are scaled by 0.936, of the lowest energy tautomer are compared to the corresponding frequencies in the infrared spectrum observed experimentally (cf. Table 8). As may be noticed the broad 2986 cm^{-1} O_2H stretching vibration in the spectrum results from the intermolecular hydrogen bonded interactions in a crystal. This has been correlated with the 3532 cm^{-1} normal vibration in the gas phase structure derived from the B3LYP/6-31G(d,p) calculations. The 3021 cm^{-1} NH stretching in the calculations is difficult to correlate with any of the vibrations in the measured infrared spectrum. Further the observed C═O and CN stretching vibrations at 1699 and 1240 cm^{-1} agree well with those predicted from theory. The downshift of the OH stretching vibration to 2986 cm^{-1} in the experimental spectrum results from the intermolecular hydrogen bonded interactions present in the crystal. Further the intramolecular hydrogen bonding causes weakening of the C═O bond of 4-amino-pent-3-ene-2-one group in the keto tautomer and shows a downshift to 1596 cm^{-1}. This vibration has been correlated with the 1586 cm^{-1} band in the observed infrared spectrum. Thus observed CO and CN stretching vibrations agree with those predicted for the gas structure of the titled ligand.

5. Conclusions

The tautomerism in 4-{[(1*Z*)-1-methyl-3-oxobut-1-enyl]amino}benzoic acid (**1**) has been investigated by employing the HF and B3LYP levels of theory. In both these tautomers intramolecular C═O···H (in keto) and C–N···H interactions (in enol tautomer) engender six membered ring formation. The enol tautomer, having strong C–N···H hydrogen bonded interactions (N···H = 1.616 Å compared to O···H = 1.750 Å in the keto tautomer) is predicted to be 17.2 kJ mol^{-1} above in energy than the keto form. The lowering of energy of the keto tautomer possibly stems from the more effective extended conjugation in near planar structure, which has been manifested in the deepest MESP minimum near carbonyl oxygen. Single crystal data from the X-ray diffraction experiment reveals the presence of C═O···H hydrogen bonds, yielding the supramolecular assemblies which is explained from the MESP topography. The observed C═O (from the carboxylic acid) and CN stretching vibrations at 1699 and 1240 cm^{-1} agree well with those predicted from theory and the latter has been correlated with the 1221 cm^{-1} vibration in the B3LYP calculations. The associated hydrogen bonded interactions

engender the downshift of OH stretching vibration to 2986 cm^{-1} in the observed infrared spectrum.

Acknowledgements

RJB wishes to acknowledge the ONR for funds to upgrade the X-ray diffractometer as well as the N1H-MBRS program for partial support. SPG is grateful to Council of Scientific and Industrial Research (CSIR), New Delhi, India, (Research Project 01(1772)/02/EMR-II). KAJ thanks CSIR for Senior Research Fellowship.

References

[1] P. Singh, R.L. Goel, B.P. Singh, J. Indian Chem. Soc. 52 (1975) 958.
[2] A.M. Mahindra, J.M. Fisher, Rabinovitz, Nature (London) 303 (1983) 64.
[3] P.R. Patel, B.T. Thakur, S. Zele, Indian J. Chem. A38 (1999) 563.
[4] E.M. Hodnett, W.J. Dunn, J. Med. Chem. 13 (1970) 768.
[5] E.M. Hodnett, P.D. Mooney, J. Med. Chem. 13 (1970) 786.
[6] E.M. Hodnett, W.J. Dunn, J. Med. Chem. 15 (1972) 339.
[7] S. Bhattacharya, S.S. Mandal, J. Chem. Soc. Chem. Commun. 1995; 2489.
[8] S. Routier, J.L. Bernier, M.J. Waring, P. Coloson, C. Houssier, C. Bailly, J. Org. Chem. 61 (1996) 2326.
[9] M. Nielsen, K.V. Gothelf, J. Chem. Soc. Perkin. Trans. 1 2001; 2440.
[10] P.R. Woodman, I.J. Munslow, P.B. Hitchcock, P. Scott, J. Chem. Soc. Dalton Trans. 1999; 4069.
[11] SMART (Version 5.624) and SHELXTL (Version 5.10); Bruker AXS Inc., Madison, WI, 2001.
[12] M.J. Frisch, G.W. Trucks, H.B. Schlegl, P.M.W. Gill, B.G. Johnson, M.A. Robb, J.R. Cheeseman, T. Keith, G.A. Petersson, J.A. Montgomery, K. Raghavachari, M.A. Al-Laham, V.G. Zakrzewski, J.V. Ortiz, J.B. Foresman, J. Ciosloski, B.B. Stefanov, A. Nanayakkara, M. Challacombe, C.Y. Peng, P.Y. Ayala, W. Chen, M.W. Wong, J.L. Andres, E.S. Replogle, R. Gomperts, R.L. Martin, D.J. Fox, J.S. Binkley, D.J. Defrees, J. Baker, J.P. Stewart, M. HeadGordon, C. Gonzalez, J.A. Pople, GAUSSIAN 94. Gaussian Inc., Pittsburgh, PA, 1995.
[13] P. Pulay, Mol. Phys. 17 (1969) 197.
[14] A.D. Becke, J. Chem. Phys. 98 (1993) 5684.
[15] C. Lee, W. Yang, R.G. Parr, Phys. Rev. B 37 (1988) 785.
[16] A.C. Limaye, S.R. Gadre, Curr. Sci. (India) 80 (2001) 1298.
[17] S.R. Gadre, R.N. Shirsat, Electrostatics of Atoms and Molecules, Universities Press, Hyderabad (India), 2000.
[18] S.R. Gadre, I.H. Shrivastava, J. Chem. Phys. 94 (1991) 4384.
[19] S.R. Gadre, S.A. Kulkarni, I.H. Shrivastava, J. Chem. Phys. 96 (1992) 5253.